

SAR Image Segmentation Based on Level Set Approach and \mathcal{G}_A^0 Model

Regis C. Pinheiro Marques, Fátima N. Medeiros, and Juvencio Santos Nobre

Abstract—This paper proposes an image segmentation method for synthetic aperture radar (SAR), exploring statistical properties of SAR data to characterize image regions. We consider \mathcal{G}_A^0 distribution parameters for SAR image segmentation, combined to the level set framework. The \mathcal{G}_A^0 distribution belongs to a class of \mathcal{G} distributions that have been successfully used to model different regions in amplitude SAR images for data modeling purpose. Such statistical data model is fundamental to deriving the energy functional to perform region mapping, which is input into our level set propagation numerical scheme that splits SAR images into homogeneous, heterogeneous, and extremely heterogeneous regions. Moreover, we introduce an assessment procedure based on stochastic distance and the \mathcal{G}_A^0 model to quantify the robustness and accuracy of our approach. Our results demonstrate the accuracy of the algorithms regarding experiments on synthetic and real SAR data.

Index Terms—Speckle, SAR image, segmentation, level sets, energy functional, G-amplitude zero distribution.

1 INTRODUCTION

A synthetic aperture radar (SAR) system is a type of imaging device that employs coherent illumination and, as laser and ultrasound, is affected by speckle noise. In SAR image processing, the return is modeled as the product of speckle noise and radar cross section. This multiplicative model [1] is widely used because the adequacy to real SAR data and the speckle noise are modeled as inherent to the acquisition process. Therefore, SAR image applications in region boundary and target detection become more difficult and may require speckle filtering. Thus, when speckle filtering is required, one can apply efficient methods [2], [3], [4], [5], [6], [7], [8], [9], [10] available in the literature.

Regarding SAR image segmentation, level set methods constitute an important class of algorithms which are based on the Hamilton-Jacobi formulation [11]. Level set methods allow efficient formulations of segmentation criteria by deriving propagation function terms as discussed in [12]. Classical methods present expensive computational effort, but recent fast level set implementations [13], [14] have configured interesting alternatives with low computation cost.

Important aspects from level set methods, such as the propagation model, can be used to design SAR image segmentation algorithms. This propagation function can incorporate speckle statistics, as gamma and square root of gamma laws [15], that have been widely used for homogeneous region segmentation in SAR images. Ayed et al. [16] devised a scheme to partition SAR images into multiple

homogeneous regions, arbitrarily modeled by gamma distributions. Although the problem of multiregion segmentation is solved, this scheme still requires the number of regions as input. Shuai and Sun [17] improved the method proposed in [16] by employing an efficient criterion for the front propagation convergence. Marques et al. [18] introduced a similar framework for target detection in speckled images that incorporates speckle statistics over local regions. These authors adopted the square root of gamma to model homogeneous regions and an adaptive windowing scheme to measure the local homogeneity [2], [6], [7].

More recently, novel SAR data models have presented advantages as \mathcal{K} , \mathcal{G} , and \mathcal{G}_A^0 distributions [19]. While the classical laws are limited to the homogeneous region characterization, the recent ones present more attractive features for data modeling [20]. The \mathcal{G}_A^0 law allows modeling of homogeneous, heterogeneous, and highly heterogeneous amplitude SAR data. This family of distributions provides a set of parameters that can characterize different regions in a SAR image. Information of \mathcal{G}_A^0 distribution parameters can be widely used to design SAR image processing and classification techniques. In [21], Mejail et al. introduced a supervised SAR data classifier which is based on its parameter maps and achieves interesting results. Gambini et al. [22] used a parameter of this distribution to quantify the SAR data roughness to detect edges through active contours and B-spline interpolation. However, this technique needs an initial segmentation step and presents topological limitation. In general, active contours methods do not address the issue of disconnected region segmentation [16].

This paper introduces a new level set algorithm to achieve the goal of segmenting homogeneous, heterogeneous, and extremely heterogeneous regions of SAR images. Our approach adopts the \mathcal{G}_A^0 distribution to model speckled data since parameters of \mathcal{G}_A^0 distribution are able to characterize the homogeneity and scale of SAR data. These distribution parameters are estimated over each domain

• The authors are with the Departamento de Engenharia de Teleinformática, Universidade Federal do Ceará, Centro de Tecnologia, Cx. Postal 6007, Campus do Pici, s/n, Fortaleza, CE, Brasil.

E-mail: regismarques@ifce.edu.br, {fsombra, juvencio}@ufc.br.

Manuscript received 27 Apr. 2011; revised 14 Nov. 2011; accepted 11 Dec. 2011; published online 22 Dec. 2011.

Recommended for acceptance by T. Tuytelaars.

For information on obtaining reprints of this article, please send e-mail to: tpami@computer.org, and reference IEEECS Log Number TPAMI-2011-04-0266.

Digital Object Identifier no. 10.1109/TPAMI.2011.274.

point, and from this information we derive an energy functional to drive the front propagation within a level set segmentation framework. This functional is accomplished by maximizing the mean energy variations between regions. The final level set stage achieves SAR image segmentation according to the energy bands.

Another contribution of this paper is the stochastic assessment methodology to evaluate the algorithms regarding the difficulty of segmentation and the ability to partition regions correctly. The proposed stochastic measures are useful to quantify the performance of segmentation methods. Moreover, these measures are of particular interest when using real SAR images where the reference or ground truth may not be available.

The remainder of the paper is organized as follows: In the next section, we review speckled data models and the parameter estimation methods with emphasis on the sample moments method. Section 3 presents the proposed level set segmentation approach based on a statistical mapping of SAR image regions. In addition, this section introduces a set of stochastic measures to evaluate the experiments. In Section 4, we present the experimental results and the stochastic evaluation methodology. Section 5 draws the conclusions and summarizes our contribution and further work.

2 BACKGROUND ON SPECKLED DATA MODELS

This section briefly presents a description of SAR data models which are mainly based on the results presented in [19], [21], [22], [23], [24], [25], [26]. Parameter estimation and interpretation are also discussed to point out its applicability in characterizing SAR data.

The SAR system return Z is adopted to follow the multiplicative model [2], [15], [21], [22], $Z = X \cdot Y$, where the backscatter X and noise Y are independent random variables. For multilook amplitude SAR images, three main models have testified the usefulness [19]: the square root of gamma ($\sqrt{\Gamma}$), whenever the area is homogeneous to the sensor, and the \mathcal{K} amplitude (\mathcal{K}_A) and \mathcal{G} amplitude-zero (\mathcal{G}_A^0), for heterogeneous and extremely heterogeneous areas, respectively. These models are particular cases of the \mathcal{G} amplitude distribution (\mathcal{G}_A), which is characterized by the density, for $z > 0$,

$$f_{\mathcal{G}_A}(z; \alpha, \gamma, \lambda, n) = \frac{2n^n(\lambda/\gamma)^{\alpha/2}}{\Gamma(n)K_\alpha(2\sqrt{\lambda\gamma})} z^{2n-1} \times \left(\frac{\gamma + nz^2}{\lambda}\right)^{(\alpha-n)/2} \times K_{\alpha-n}(2\sqrt{\lambda(\gamma + nz^2)}), \quad (1)$$

where n is the number of looks, $K_e(\cdot)$ denotes the third kind modified Bessel function of order e , and $\Gamma(\cdot)$ is the gamma function. The parameter space of α , γ , and λ is expressed by

$$\begin{aligned} \gamma &> 0, \lambda \geq 0 \text{ if } \alpha < 0; \\ \gamma &> 0, \lambda > 0 \text{ if } \alpha = 0; \\ \gamma &\geq 0, \lambda > 0 \text{ if } \alpha > 0. \end{aligned} \quad (2)$$

Table 1 presents the relation between the distributions that model amplitude SAR data, where \xrightarrow{D} and \xrightarrow{P} denote convergence of the random variable Z in distribution and

TABLE 1
Models for Amplitude SAR Data [19]

$\mathcal{G}_A(z; \alpha, \gamma, \lambda, n)$	$\alpha, \lambda > 0$ $\gamma \rightarrow 0$ \xrightarrow{D}	Heterogeneous $\mathcal{K}_A(\alpha, \lambda, n)$	$\alpha, \lambda \rightarrow \infty$ $\alpha/\lambda \rightarrow \beta$ \xrightarrow{P}	Homogeneous $\sqrt{\Gamma}(n, n/\beta)$
	\xrightarrow{D}	$\mathcal{G}_A^0(\alpha, \gamma, n)$ Highly	\xrightarrow{P}	$\sqrt{\Gamma}(n, n\zeta)$
	$\lambda \rightarrow 0$ $-\alpha, \gamma > 0$	Heterogeneous	$-\alpha/\gamma \rightarrow \zeta$ $-\alpha, \gamma \rightarrow \infty$	Homogeneous

probability, respectively. Under certain conditions of the parameter space [19], the \mathcal{G}_A law converges in distribution to a \mathcal{K} -Amplitude (\mathcal{K}_A), which models heterogeneous regions in SAR images. The \mathcal{K}_A distribution is characterized by the density function

$$f_{\mathcal{K}_A}(z; \alpha, \lambda, n) = \frac{4\lambda n z}{\Gamma(\alpha)\Gamma(n)} (\lambda n z^2)^{(\alpha+n)/2-1} \times K_{\alpha-n}(2z\sqrt{\lambda n}), \quad (3)$$

$\alpha, \lambda, n, z > 0$.

For homogeneous regions in SAR images, the \mathcal{K}_A law converges in probability to a square root of gamma with the generalized parameter β [19]. The $\sqrt{\Gamma}$ density function is given by

$$f_{\sqrt{\Gamma}}(z; n/\beta, n) = \frac{2n^n}{\beta^n \Gamma(n)} z^{2n-1} \exp(-nz^2/\beta), \quad (4)$$

$z, n > 0$.

Frery et al. [19] introduced another particular case of \mathcal{G}_A distribution to model the amplitude data return Z , specially in the case of heterogeneous and extremely heterogeneous areas [23]. This distribution, named \mathcal{G}_A^0 , configures an interesting alternative to describe the observed data. Allend et al. emphasized in [27] that this law was lately accepted to model homogeneous regions.

The \mathcal{G}_A^0 distribution is characterized by the density function

$$f_{\mathcal{G}_A^0}(z, \alpha, \gamma, n) = \frac{2n^n \Gamma(n - \alpha)}{\gamma^\alpha \Gamma(-\alpha) \Gamma(n)} \frac{z^{2n-1}}{(\gamma + z^2 n)^{n-\alpha}}, \quad (5)$$

$-\alpha, \gamma, z > 0, n \geq 1$.

The theoretical moments of order r exist if $\alpha < -r/2$, while $\gamma > 0$ and $n \geq 1$, and they are given by

$$E_{\mathcal{G}_A^0}(Z^r) = \left(\frac{\gamma}{n}\right)^{r/2} \frac{\Gamma(-\alpha - r/2) \Gamma(n + r/2)}{\Gamma(-\alpha) \Gamma(n)}. \quad (6)$$

The \mathcal{G}_A^0 cumulative distribution is defined as

$$F_{\mathcal{G}_A^0}(z) = \Upsilon_{2n, -2\alpha} \left(\frac{-\alpha z^2}{\gamma} \right), \quad (7)$$

where $\Upsilon_{2n, -2\alpha}$ is the cumulative distribution function of Snedecor's F law with $2n$ and -2α degrees of freedom.

The $\sqrt{\Gamma}$ and the \mathcal{K}_A models present mathematical restrictions to solve the cumulative distribution function. In other words, the \mathcal{G}_A^0 cumulative distribution function is quite tractable as (7) presents the available computational solution, as well as its inverse ($F_{\mathcal{G}_A^0}^{-1}(z)$). The functions Υ and

Υ^{-1} are available in statistical software platforms and important results can be achieved, as the sample simulation of $Z \sim f_{\mathcal{G}_A^0}(z, \alpha, \gamma, n)$, presented in [28] as

$$Z = \sqrt{-\frac{\gamma}{\alpha} \Upsilon_{2n, -2\alpha}^{-1}(U)}, \quad (8)$$

where U is a uniformly distributed random variable in $(0, 1)$.

2.1 \mathcal{G}_A^0 Parameter Estimation and Interpretation

Due to the advantages of the \mathcal{G}_A^0 model, we have assumed that $Z \sim f_{\mathcal{G}_A^0}(z, \boldsymbol{\theta}, n)$, where $\boldsymbol{\theta} = (\alpha, \gamma)$ is the parameter vector of the \mathcal{G}_A^0 distribution. The parameters α and γ of the \mathcal{G}_A^0 distribution can be used to characterize SAR image aspects of roughness and scale [19], respectively. In addition, it has been observed that for $\alpha \rightarrow 0^-$, data present highly heterogeneous gray levels. On the other hand, over homogeneous areas of SAR images, $\alpha \rightarrow -\infty$. The scale parameter γ is proportional to the backscatter amplitude.

Estimation of the \mathcal{G}_A^0 parameters has been extensively discussed in the literature. Statistical methods can be applied as the method of moments (MO) [23], [19], [21], maximum likelihood (ML) [28], and robust estimators [24], [27]. In general, the aforementioned estimation techniques present similar limitations because analytical solutions are not achieved and numerical problems can arise.

Regarding MO, it can be easily and successfully applied to estimate the \mathcal{G}_A^0 distribution parameters [20] and under weak regularity condition, also supplies consistent estimators [29].

The ML estimation method is consistent and it presents optimal properties. However, as observed by Mejail et al. [21], order statistics and ML methods lead to numerical problems whenever the estimation is performed in small samples over homogeneous areas. In addition, the computation time required to perform the parameter estimation is another relevant problem [15].

The current approach should perform a large number of estimation experiments (for each image pixel) using small samples. The use of large samples obtained with large windows usually cause heavy blurring in resulting data [28]. To overcome these drawbacks, the strategy for parameter estimation adopted in [21] is followed. Accordingly, to estimate the roughness parameter, we search for a numerical solution of the relationship

$$\frac{\Gamma^2(-\hat{\alpha} - 1/4)}{\Gamma(-\hat{\alpha})\Gamma(-\hat{\alpha} - 1/2)} - \frac{m_{1/2}^2 \Gamma(n)\Gamma(n+1/2)}{m_1 \Gamma^2(n+1/4)} = 0, \quad (9)$$

where m_r denotes the r th-order sample moment. The estimated scale parameter ($\hat{\gamma}$) is obtained by replacing $\hat{\alpha}$ in (6) for $r = 1$ and $E_{\mathcal{G}_A^0}(z) = \hat{m}_1$. Given the impossibility of obtaining analytically the standard errors of the estimators, we can use the Bootstrap methods to obtain them. For details, see [30], for example.

The number of looks, n , is generally an integer provided by the sensor and in this paper it is an a priori information. However, in the absence of it, the number of looks can be estimated from real data and it is therefore interesting to call the *equivalent number of looks* (\hat{n}) [19].

Since homogeneous regions follow the $\sqrt{\Gamma}$ law, the MO method can be used to solve the following equation [18]:

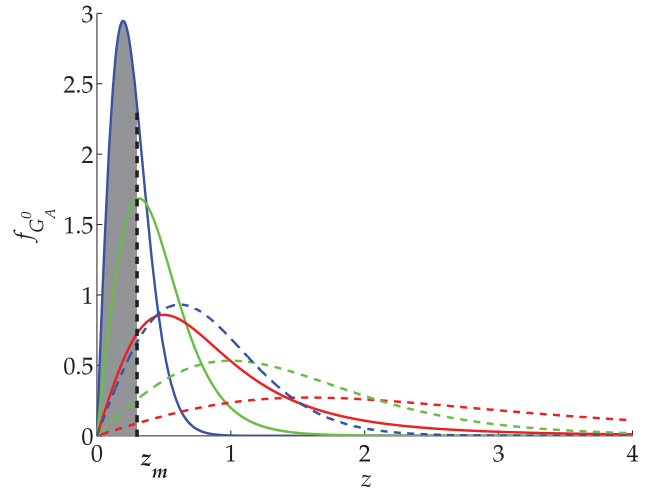


Fig. 1. Two families of $\mathcal{G}_A^0(z, \alpha, \gamma, 1)$ distributions for $\gamma = 1$ (solid lines) and $\gamma = 10$ (dashed lines) with three different roughness patterns: homogeneous $\alpha = -12.5$ (blue lines), heterogeneous $\alpha = -4.5$ (green lines), and extremely heterogeneous $\alpha = -1.5$ (red lines).

$$\left(\sqrt{\frac{m_2}{\hat{n}}} \right) \frac{\Gamma(\hat{n} + \frac{1}{2})}{\Gamma(\hat{n})} - m_1 = 0. \quad (10)$$

3 THE PROPOSED LEVEL SET FRAMEWORK

3.1 Energy Functional Map

Let $Z : \Theta \rightarrow \mathbb{R}$ be the amplitude SAR image, where $\Theta = \{\mathbf{x} = (i, j); i, j \in \mathbb{Z}\}$. We can define the set of image regions $\mathcal{R} = \{\Omega_i; \Omega_i \subset \Theta\}$, which is disjoint ($\Omega_i \cap \Omega_j = \emptyset, i \neq j$) and covers the domain ($\cup_{i=1}^N \Omega_i = \Theta$).

Following propositions stated in [31], samples of distinct image regions are described by distinct distributions. If $\Omega_i, \Omega_j \subset \Theta$ are different regions of SAR image, the random variables $Z_i : \Omega_i \rightarrow \mathbb{R}$ and $Z_j : \Omega_j \rightarrow \mathbb{R}$ are \mathcal{G}_A^0 distributed with distinct parameter vectors $\boldsymbol{\theta}_i$ and $\boldsymbol{\theta}_j$, respectively. Furthermore, over any point $P \in \Omega_i$, a vector of parameters $\hat{\boldsymbol{\theta}}_P$ can be estimated such that $\hat{\boldsymbol{\theta}}_P \approx \boldsymbol{\theta}_i$ and, consequently, $Z_i \sim f_{\mathcal{G}_A^0}(z, \hat{\boldsymbol{\theta}}_P, n)$.

As hinted earlier, it is also reasonable to expect that any other point $Q \in \Omega_i$ presents similar roughness and scale patterns. Thus, for two distinct points $P, Q \in \Omega_i$, the relationship between probability ($P(z \leq z_m) = F_{\mathcal{G}_A^0}(z_m, \hat{\boldsymbol{\theta}}, n)$) is

$$F_{\mathcal{G}_A^0}(z_m, \hat{\boldsymbol{\theta}}_P, n) \approx F_{\mathcal{G}_A^0}(z_m, \hat{\boldsymbol{\theta}}_Q, n). \quad (11)$$

In other words, if $P \in \Omega_i$ and $Q \in \Omega_j$, $\hat{\boldsymbol{\theta}}_P$ and $\hat{\boldsymbol{\theta}}_Q$ characterize distinct regions; consequently, the cumulative distributions are distinct. Based on the unicity of the cumulative distribution (CDF), we observed that it can be used to differentiate probability distributions that model different regions. The highlighted areas, under the curves, in Fig. 1 show the discrimination ability of this function. Under this assumption, we designed an energy functional in terms of roughness and scale characteristics, to map differences between distinct regions. Thus, this functional is given by

$$\mathcal{E}(\hat{\boldsymbol{\theta}}; n, z_m) = \Upsilon_{2n, -2\hat{\alpha}} \left(-\frac{\hat{\alpha}}{\hat{\gamma}} z_m^2 \right). \quad (12)$$

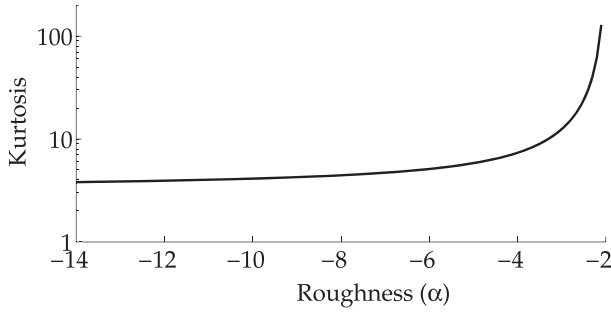


Fig. 2. Kurtosis of $f_{\mathcal{G}_A^0}(\alpha, \cdot, 1)$ distribution.

The roughness and scale parameters can be estimated over all pixels $\mathbf{x} \in \Theta$, and two parameter maps ($\alpha(\mathbf{x})$ and $\gamma(\mathbf{x})$) are derived as in [21]. Thus, an *energy map* is defined from (12) as

$$\mathcal{E}_{\mathbf{x}} = \mathcal{E}(\hat{\boldsymbol{\theta}}(\mathbf{x}); n, z_m), \quad (13)$$

where n and z_m are constant in Θ . Fig. 1 shows two families of \mathcal{G}_A^0 distributions for different roughness values. The area under the curves corresponds to the energy value $\mathcal{E} = F_{\mathcal{G}_A^0}(\boldsymbol{\theta}; n, z_m)$. As observed in Fig. 1, when $\alpha \rightarrow -1$, the data are extremely heterogenous and $\mathcal{E} \ll 1$. Otherwise, if $\alpha \rightarrow -\infty$, then $\mathcal{E} \rightarrow 1$. These relations can be summarized by analyzing the skewness and the kurtosis of the distribution. The former is presented in [21] and the latter is derived in Appendix B, which can be found in the Computer Society Digital Library at <http://doi.ieeecomputersociety.org/10.1109/TPAMI.2011.274>.

The kurtosis in (39) (see Appendix B, available in the online supplemental material) increases with the roughness parameter, and it does not depend on γ , as observed in Fig. 2. This result is directly implicated in a relation between the increase of probability and the decrease of roughness parameter. However, scale parameter increments lead to variations of the distribution function and consequently decrement the energy, as (12) specifies.

Such considerations lead us to suppose that amplitude of energy variations should reach the highest values over region boundaries. However, these fluctuations are limited to low values within regions. Thus, energy oscillations over region boundaries can be evaluated from the total energy variation:

$$\mathcal{C} = \sum_{\mathbf{x} \in \Theta} |\nabla \mathcal{E}_{\mathbf{x}}|, \quad (14)$$

where $|\nabla \mathcal{E}_{\mathbf{x}}|$ is the magnitude of the spatial gradient, which is given by

$$\left| \frac{\partial \mathcal{E}_{\mathbf{x}}}{\partial \mathbf{x}} \right| = \left| \frac{\partial z}{\partial \mathbf{x}} \right| \left| \frac{\partial \mathcal{E}_{\mathbf{x}}}{\partial z} \right|. \quad (15)$$

As $\frac{\partial z}{\partial \mathbf{x}} = \nabla Z$ is the image gradient and $\frac{\partial \mathcal{E}_{\mathbf{x}}}{\partial z}$ represents the derivative of the cumulative distribution function, we can write the total energy variation as

$$\mathcal{C} = \sum_{\mathbf{x} \in \Theta} |\nabla Z| \cdot f_{\mathcal{G}_A^0}(z, \hat{\boldsymbol{\theta}}(\mathbf{x}), n) \quad (16)$$

and the novel functional provides the maximal discrimination when

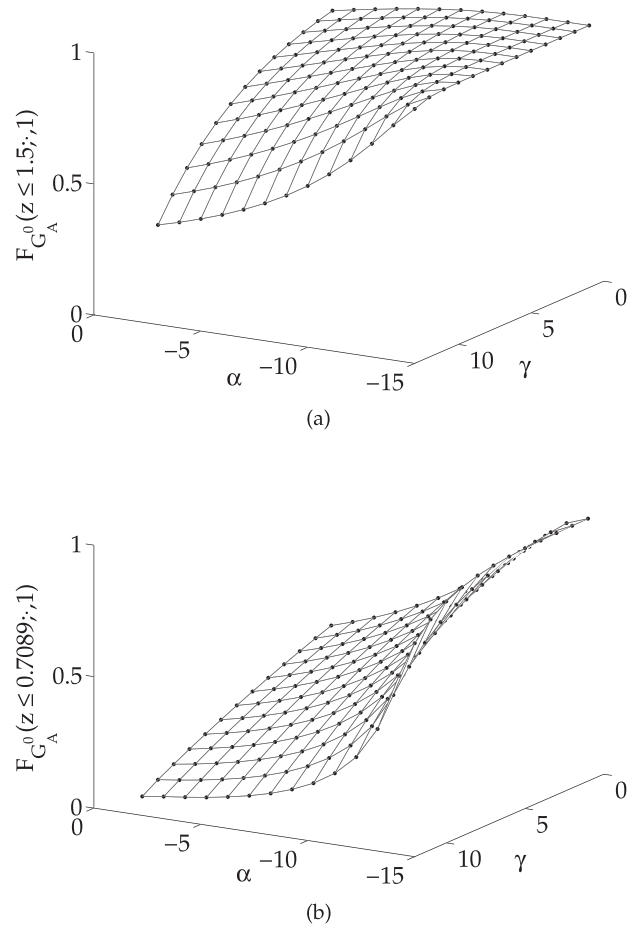


Fig. 3. Behavior of the cumulative distribution function for (a) an arbitrary parameter $z_m = 1.5$ and (b) the estimate provided by proposed method ($z_m = 0.7089$).

$$z_m = \arg \max_z \{\mathcal{C}\}. \quad (17)$$

Fig. 3a shows the behavior of the functional for several parameter vectors ($\boldsymbol{\theta}$) and an arbitrary $z_m = 1.5$. Fig. 3b presents the energy values computed in accordance with the proposed criterion where $z_m = 0.7089$. The surface in Fig. 3b presents superior curvature and thus it suggests a better discrimination between the parameter vectors.

Fig. 4a shows a synthetic SAR image where four samples were simulated under a family of the \mathcal{G}_A^0 laws. The scale parameter γ is set from top to down to 100 and 1,000, respectively. The roughness parameter is set to $\alpha = -4.5$ (left) and $\alpha = -1.5$ (right). These values represent highly heterogeneous and heterogeneous data, respectively. Figs. 4b and 4c illustrate the estimated roughness and scale maps, respectively. The computed energy map can be observed in Fig. 4d and it is worth noting that this novel map improves image region discrimination. To improve visualization, images displayed in Figs. 4a, 4b, and 4c present contrast enhancement, whereas the one in Fig. 4d is not enhanced.

In accordance with Mejail et al. [21], the scale parameter can be used to discriminate different targets in areas with a similar roughness pattern. Otherwise, the roughness parameter provides relevant information for the segmentation of image clutters [22]. As a matter of fact, both the roughness

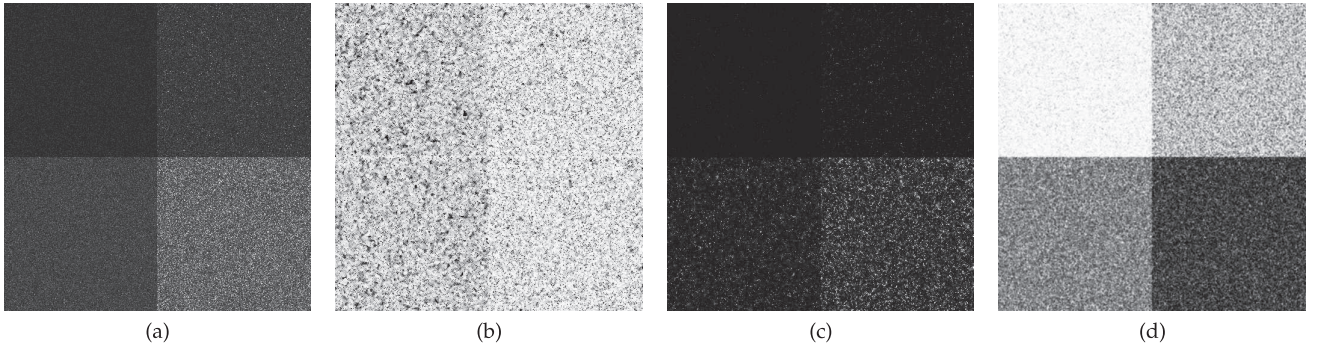


Fig. 4. (a) Synthetic SAR data modeled by a family of four \mathcal{G}_A^0 functions with parameters set to $n = 1$, $\gamma \in 100, 1,000$, and $\alpha \in -1.5, -4.5$ and estimated maps of (b) negative roughness ($-\alpha$), (c) scale (γ), and (d) energy (\mathcal{E}).

and scale parameters are necessary to design efficient discriminants for SAR image regions. Based on this assumption and that z_m can be properly estimated, the energy functional can discriminate image regions with different roughness and scale patterns.

3.1.1 Algorithm Issues

Algorithm 1 summarizes the main steps to compute the novel energy functional.

Algorithm 1. Energy map estimation

- 1: $WindowSize \leftarrow 3$;
- 2: $n \leftarrow NumberOfLooks$;
- 3: **for** each $\mathbf{x} \in \Theta$ **do**
- 4: Compute $\hat{m}_1(\mathbf{x})$ and $\hat{m}_{1/2}(\mathbf{x})$;
- 5: Solve Equation (9) to obtain the parameter $\hat{\alpha}(\mathbf{x})$;
- 6: Solve Equation (6) with $r = 1$ or $r = 1/2$ to obtain the parameter $\hat{\gamma}(\mathbf{x})$;
- 7: **end for**
- 8: Compute the magnitude of image gradient ($|\nabla Z|$);
- 9: $z_m^{(0)} \leftarrow ImageMode$;
- 10: Find the numerical solution of $z_m \leftarrow \arg \max_z \{C\}$;
- 11: Compute \mathcal{E} in Equation (12).

Step 1 sets the neighborhood size for moments and parameter estimation, which is performed from Steps 2 to 5. We emphasize that (9) can be inconsistent with data in several points of domain; consequently, the estimative of α is not obtained. To overcome this problem, we have assigned the median taken from the neighborhood roughness to those points where the estimation fails as suggested in [22].

In Step 6, the magnitude of the SAR image gradient is computed and Step 7 returns an initial estimate of z_m . In this paper, we have assigned the mode of image histogram to the initial estimate. In addition, we have used integer format images for which the “natural” histogram is formed with bins of size 1. If a multimodal histogram is obtained, the smallest mode is used as the initial estimate. To maximize (17), in Step 8 we have used a numerical routine based on the Broyden-Fletcher-Goldfarb-Shanno method (BFGS).

3.2 The Level Set Propagation Model

The level set technique is based on solutions of variational systems [32]. In this problem, a dynamic system evaluates for minimal energy state, in accordance with a cost function f_c .

Sethian [11] formulated the level set technique from Hamilton-Jacobi equation. In this approach, each point of a closed curve $\vec{\phi}$ evolves with velocity $(\pm \frac{d\phi}{dt} \vec{n})$, where $(\pm \vec{n})$ is the unit vector that is perpendicular to $\vec{\phi}$.

In level set methods, the front $\vec{\phi}: \mathbb{R}^2 \times \mathbb{R}^+ \rightarrow \mathbb{R}$ movement is a consequence of the surface $\Psi(\mathbf{x})$ motion in which one is embedded in accordance with

$$\vec{\phi}(s, t) = \{\mathbf{x} | \Psi(\mathbf{x}, t) = 0\}, \mathbf{x} \in \mathbb{R}^n, \quad (18)$$

where $s \in \mathbb{R}^2$ is the coordinate of the parametric curve $\vec{\phi}$ and $t \in \mathbb{R}^+$ is the evolution time. This process is expressed as [11]

$$\psi^{k+1} = \psi^k + \Delta t \psi_t, \quad (19)$$

where Δt is the time step, ψ is the level set function, and ψ_t is the evolution function.

Traditionally, ψ is the signed distance transform of an initial family of curves $\vec{\phi}(s, t)_{t=0}$. The evolution function (ψ_t) is composed of a regularization term based on the curvature of ψ , a term of advection, and a propagation term ($\frac{\partial \phi}{\partial t}$). In this paper, we have adopted a Gaussian filter to regularize the level set function ψ , as suggested in [33]. A regularized version of the evolution function ψ_t is defined as [34]

$$\psi_t = \frac{\partial \phi}{\partial t} \cdot \delta_\epsilon(\psi), \quad (20)$$

where δ_ϵ is an approximation of Dirac function, expressed as

$$\delta_\epsilon(z) = \frac{1}{\pi} \cdot \frac{\epsilon}{\epsilon^2 + z^2}, \quad (21)$$

and $\epsilon \in \mathbb{R}^+$ is a regularization constant.

The process starts with a level set zero given by

$$\psi^0(\mathbf{x}) = \begin{cases} -1, & \mathbf{x} \in \Omega_1 \\ 0, & \mathbf{x} \in \partial\Omega/\partial\mathbf{x} \\ 1, & \mathbf{x} \in \Omega_2, \end{cases} \quad (22)$$

where Ω_1 and Ω_2 are the internal and the external regions, respectively, of the initial front $\vec{\phi}(s, t)_{t=0}$ and $\partial\Omega/\partial\mathbf{x}$ corresponds to the region boundaries.

The purpose of the proposed propagation function is to maximize the mean energy variation between regions. This criterion is based on the functional behavior that suggests a minimal variation within regions. After a trial and error process, we found that the linear cost function is enough for

penalizing significant energy differences between regions, without magnifying random differences within the same region. The associated cost function can be expressed as

$$f_c = \sum_{i=1}^{N-1} \sum_{j=i}^N |\mu_i - \mu_j|, \quad (23)$$

where μ_i is the mean energy of i th region and is given by

$$\mu_i = \frac{\int_{\Omega_i} \mathcal{E} dx}{\mathcal{A}(\Omega_i)} \quad (24)$$

and $\int \mathcal{E} dx$ refers to the total energy of Ω_i and $\mathcal{A}(\Omega_i)$ is the region area.

Our level set model evolves similarly to [16] and [18], where the cost function over the parametric closed curve $\vec{\phi}(s, t)$ is minimized according to the following expression:

$$\frac{d\vec{\phi}}{dt} = -\frac{\partial f_c}{\partial \vec{\phi}}. \quad (25)$$

For binary segmentation, i.e., $N = 2$, the cost function can be expressed as $f_c = \mu_1 - \mu_2$, while $\mu_1 > \mu_2$. The derivative in (25) is given by

$$\frac{\partial f_c}{\partial \vec{\phi}} = \frac{\partial}{\partial \vec{\phi}} (\mu_1 - \mu_2), \quad (26)$$

where

$$\frac{\partial \mu}{\partial \vec{\phi}} = \frac{\partial}{\partial \vec{\phi}} \left(\frac{\int_{\Omega_i} \mathcal{E} dx}{\mathcal{A}(\Omega_i)} \right). \quad (27)$$

The right term in (27) can be solved since the area derivatives are given by [16]

$$\frac{\partial}{\partial \vec{\phi}} \int u(\mathbf{x}) dx = u(\mathbf{x}) \vec{n}, \quad (28)$$

and

$$\frac{\partial \mathcal{A}(\Omega)}{\partial \vec{\phi}} = \vec{n}. \quad (29)$$

Hence,

$$\frac{\partial \mu}{\partial \vec{\phi}} = -\frac{1}{\mathcal{A}^2(\Omega)} \left(\mathcal{E} \mathcal{A}(\Omega) \vec{n} - \int_{\Omega} \mathcal{E} dx \vec{n} \right), \quad (30)$$

$$\frac{\partial \mu}{\partial \vec{\phi}} = -\frac{1}{\mathcal{A}^2(\Omega)} (\mathcal{E} \mathcal{A}(\Omega) \vec{n} - \mathcal{A}(\Omega) \mu \vec{n}), \quad (31)$$

$$\frac{\partial \mu}{\partial \vec{\phi}} = -\frac{(\mathcal{E} - \mu)}{\mathcal{A}(\Omega)} \vec{n} \Big|_{\mathbf{x} \in \Omega}, \quad (32)$$

where $\vec{n} = \nabla \vec{\phi} / |\nabla \vec{\phi}|$ is a unit vector that is perpendicular to $\vec{\phi}$.

The final evolution model is given by

$$\frac{d\vec{\phi}}{dt} = -\frac{(\mathcal{E} - \mu_1) \vec{n}}{\mathcal{A}(\Omega_1)} + \frac{(\mathcal{E} - \mu_2)(-\vec{n})}{\mathcal{A}(\Omega_2)}. \quad (33)$$

Indeed, the evolution of the level set function follows (19) with ψ_t expressed in terms of (33).

The proposed method converges if $|\bar{f}_c^k - \bar{f}_c^{k+1}| < \Delta C$, where \bar{f}_c is the mean cost in the last K_t iterations and ΔC is the convergency threshold. In the following, Algorithm 2 summarizes our proposed level set framework.

Algorithm 2. The level set evolution

- 1: $k \leftarrow 0$;
- 2: State ΔC ;
- 3: State K_t ;
- 4: State an initial partition $\mathcal{R} = \{\Omega_1, \Omega_2\}$;
- 5: Start ψ^0 according to Equation (22);
- 6: **while** $|\bar{f}_c^k - \bar{f}_c^{k+1}| < \Delta C$ **do**
- 7: Compute $\mathcal{A}(\Omega_1)$, μ_1 , $\mathcal{A}(\Omega_2)$, μ_2 ;
- 8: Compute ψ_t according to Equation (33) and (20);
- 9: Evolve ψ following Equation (19);
- 10: Smooth ψ^{k+1} with a Gaussian filter;
- 11: $k \leftarrow k + 1$;
- 12: **end while**

3.3 Stochastic Assessment Methodology

This section introduces the assessment methodology to quantify the performance of the segmentation algorithms. Our proposed evaluation measures rely on the arithmetic-geometric distance, and the tests performed to validate our methodology are assessed by these measures. According to Frery et al. [31] and Nascimento et al. [35], this distance presented the best discrimination ability to perform a contrast quantification of the speckled data with stochastic-inspired distances.

The arithmetic-geometric distance between $Z_1 \in \Omega_1$ and $Z_2 \in \Omega_2$ is given by

$$S_{AG}(Z_1, Z_2) = \frac{1}{2} \int_{\mathbb{R}^+} \left[\left(f_{\mathcal{G}_A^0}(z, \boldsymbol{\theta}_1, n) + f_{\mathcal{G}_A^0}(z, \boldsymbol{\theta}_2, n) \right) \times \log \left(\frac{f_{\mathcal{G}_A^0}(z, \boldsymbol{\theta}_1, n) + f_{\mathcal{G}_A^0}(z, \boldsymbol{\theta}_2, n)}{2 \sqrt{f_{\mathcal{G}_A^0}(z, \boldsymbol{\theta}_1, n) \times f_{\mathcal{G}_A^0}(z, \boldsymbol{\theta}_2, n)}} \right) \right] dz. \quad (34)$$

In the following, we derive evaluation measures based on the arithmetic-geometric distance (34).

Segmentation distance. It measures the statistical distance between the segmentation result and the reference region. From (34), we derived it as

$$SD = S_{AG}(Z_f^r, Z_f^s), \quad (35)$$

where $Z_f^r \in \Omega_f^r$ is the reference foreground and $Z_f^s \in \Omega_f^s$ is the segmented region.

Difficulty of segmentation. It quantifies the difficulty to segment foreground (Ω_f) and background (Ω_b). When the region contrast is low, it implies an $S_{AG}(Z_f, Z_b)$ decrement; consequently, the segmentation difficulty increases. The difficulty measure can be expressed by

$$DoS = \frac{1}{S_{AG}(Z_f, Z_b)}. \quad (36)$$

Cross-region fitting. It combines both the segmentation distance and the difficulty of segmentation to quantify the



Fig. 5. Examples of the Monte Carlo experiment results.

ability of the method to partition regions correctly. It is given by

$$CRF = \frac{1}{1 + \sqrt{DoS \times |S_{AG}(Z_f^r, Z_b^s) - S_{AG}(Z_f^s, Z_b^r)|}}. \quad (37)$$

Although the difficulty of segmentation and segmentation distance measures can assess segmentation methods, they are relative quantities. Alternatively, the cross-region fitting error evaluates the segmentation algorithms taking into account the reference parameters θ_f^r and θ_b^r regardless of the reference or the ground-truth image. This measure is of particular interest when using real SAR images where the reference or ground truth may not be available.

Attempting to provide a reference measure when segmenting synthetic data, we propose the *Region Fitting Error*, which is given by

$$RFE = \frac{\max(\mathcal{A}(\Omega_r), \mathcal{A}(\Omega_s)) - \mathcal{A}(\Omega_r \cap \Omega_s)}{\max(\mathcal{A}(\Omega_r), \mathcal{A}(\Omega_s))}. \quad (38)$$

The *region fitting error* provides a quantitative difference between the segmented foreground region area $\mathcal{A}(\Omega_s)$ and the reference one $\mathcal{A}(\Omega_r)$. The *RFE* is a modified version of the *success of shape fit* measure that leads to a computational error if $\mathcal{A}(\Omega_r \cup \Omega_s) = 0$ [36].

4 EXPERIMENTAL RESULTS

To evaluate the novel method, we have compared it to other SAR image segmentation methods based on level sets [16], [37]. All methods and evaluation measures were developed by using the MatLab platform.

4.1 Synthetic Speckled Image Segmentation

4.1.1 Monte Carlo Experiment

The simulation tests were conducted by a Monte Carlo experiment where samples of SAR data were generated using a set of 49 binary images with variable geometry and size. The speckled images were processed by the convergence criterion $\Delta C = 10^{-7}$ and parameter set: $K_t = 50$, $\Delta t = 0.05$, $\epsilon = 1.0$, and $\sigma = 0.5$, for the level set method.

The foreground and the background regions followed distinct distributions $\mathcal{G}_A^0(\alpha_f, \gamma_f, n)$ and $\mathcal{G}_A^0(\alpha_b, \gamma_b, n)$, respectively. The parameters were $\alpha \in \{-1.5, -3, -8\}$, $\gamma \in \{1, 10, 100\}$, and $n \in \{1, 3, 6\}$. The following three contexts were tested:

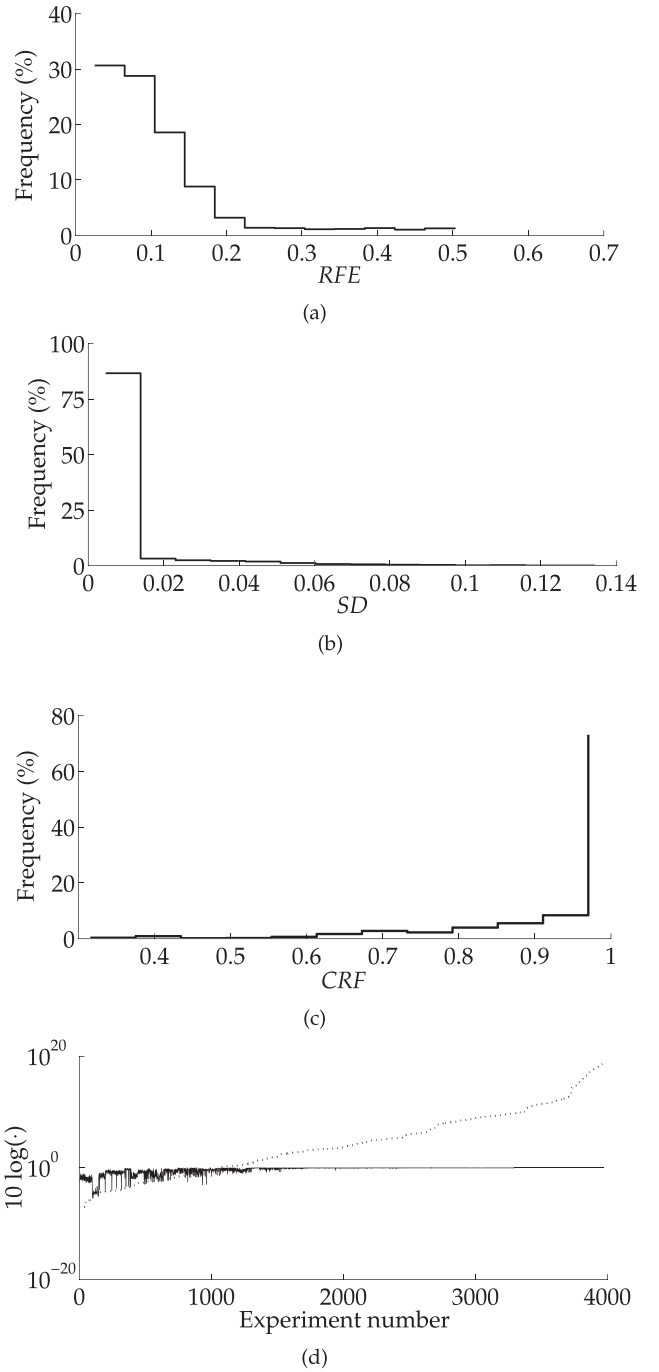


Fig. 6. Monte Carlo experiment evaluation: (a) segmentation error (*RFE*), (b) segmentation distance (*SD*), (c) region fitting (*CRF*), and (d) *CRF* (solid line) versus test difficulty (dotted line).

- $\alpha_f > \alpha_b$ and $\gamma_f > \gamma_b$,
- $\alpha_f < \alpha_b$ and $\gamma_f = \gamma_b$,
- $\alpha_f = \alpha_b$ and $\gamma_f = 20\gamma_b$,

and for each one, 27 distinct contamination patterns were replicated by using the set of 49 binary images. The Monte Carlo experiment consisted of 3,969 tests such that each context presented 1,323 tests. Fig. 5 shows some segmentation results which were chosen among the best ones. Fig. 6 illustrates the evaluation of the experiments in histograms of the *RFE* and the stochastic measures.

For the same set of parameters, the proposed method converged in 93 percent of the tests, which corresponds to

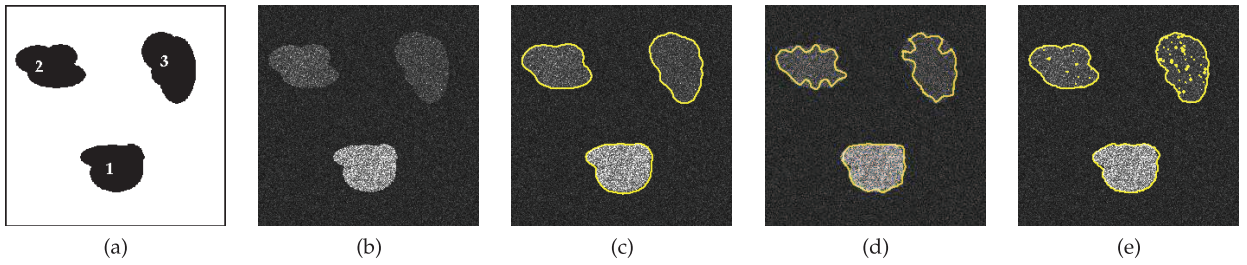


Fig. 7. Segmentation result for a synthetic SAR image: (a) ground truth or image region reference, (b) simulated SAR image following a family of $\mathcal{G}_A^0(\alpha, 1, 8)$ distribution, (c) result of the proposed method, and (d)-(e) the results of the methods introduced in [16] and [37], respectively.

TABLE 2
CRF and RFE for Speckled Versions of Image in Fig. 7a

n	Region	DoS	CRF			RFE		
			[16]	[37]	Proposed Method	[16]	[37]	Proposed Method
1	#1	1.5768	0.7407	0.8803	0.8203	0.9817	0.0619	0.0783
	#2	9.6774	0.6080	0.7032	0.9162	0.6731	0.2719	0.0335
	#3	16.7771	0.5420	0.6203	0.7628	0.8741	0.5704	0.1422
2	#1	0.7581	0.6514	0.7623	0.9139	0.6587	0.0736	0.0251
	#2	4.6473	0.6897	0.7660	0.8261	0.4992	0.2091	0.0782
	#3	8.5541	0.5762	0.6886	0.6974	0.6599	0.3564	0.2428
3	#1	0.5517	0.7712	0.8307	0.9222	0.0887	0.0626	0.0330
	#2	2.9838	0.6533	0.7462	0.8244	0.6096	0.2032	0.0606
	#3	6.1366	0.5818	0.7500	0.7647	0.8037	0.4266	0.1756
8	#1	0.2562	0.9322	0.7450	0.8688	0.0395	0.0657	0.0418
	#2	1.2819	0.7778	0.8835	0.9191	0.3178	0.0280	0.0306
	#3	2.6293	0.7638	0.8992	0.8300	0.4097	0.0729	0.0856

3,691 experiments out of 3,969. This performance can be improved by adjusting the ϵ , Δt , and σ parameters. One can observe from the RFE histogram displayed in Fig. 6a that about 80 percent of the tests presented error around 0.1, with minimum and maximum errors around 0.0054 and 0.5070, respectively. The SD and the CRF histograms in Figs. 6b and 6c point out similar results.

From the Monte Carlo procedure, we can conclude that the results in Figs. 6a, 6b, and 6c show that the stochastic distance emphasizes the outperformance of the proposed method. Moreover, the histograms of SD and CRF indicate the segmentation accuracy of the methods. The comparative analysis between CRF and DoS in Fig. 6d shows the ability of method to partition regions in images of very low contrast (hard tests).

4.1.2 Comparative Analysis of Level Set Methods for Synthetic Data

Fig. 7b displays a synthetic speckled image of 256×256 pixels. It simulates an image with four different return

patterns, using the $\mathcal{G}_A^0(\alpha, 1, 8)$ law with homogeneous background ($\alpha = -10$) and three spots with varying degrees of roughness ($\alpha = -1.5, -4, -5$). It is also important to note that the improvement in image visualization is due to contrast enhancement.

The simulated patterns tend to present an increasing segmentation difficulty from region Ω_1 to Ω_3 , and this aspect arises from the distinct roughness parameter (α) values.

The performance of the level set method in [16] was not adequate in accordance with the segmentation result exhibited in Fig. 7d, which failed in detecting regions #2 and #3. The method in [37] was accurate, as can be observed in Fig. 7e. However, residual noise of the segmentation process remained. The performance of these methods was inferior especially in low contrast region (#2 and #3) segmentation, while the proposed method correctly detected all region edges, as Fig. 7c illustrates. The numerical results in Table 2 point out the best performance of the proposed method for different difficulty levels. In general,

TABLE 3
Average Speed of Methods Convergence

Method	Number of iterations	CPU time (s)
[16]	637.5	7.2954
[37]	1350	8.8823
Proposed method	607.5	7.4089

the proposed method results presented the minimum RFE values and a superior separability (CRF) of regions with distinct statistical properties, mainly for high DoS values.

The preliminary segmentation results showed that an efficient set of measures that encompass RFE , DoS , and CRF can quantify the accuracy, the test difficulty, and the correct partition of regions based on their statistical features. Furthermore, DoS and CRF can be applied to

real SAR image segmentation results by choosing appropriate reference samples of the background and the foreground.

Table 3 shows the average values of the computational time and level set iterations number for experiments summarized in Table 2, which were performed on a 2.4 GHz CPU with 4 GB RAM. The methods based on the level set techniques present similar results. However, the propagation model proposed in [37] requires empirical parameters leading to several attempts to segment the image. Moreover, the convergence criterion of the algorithms in [16] and [37] is unknown and an adequate number of iterations are needed to achieve the process. The proposed method required additional time to execute Algorithm 1 for energy map computation; however, the

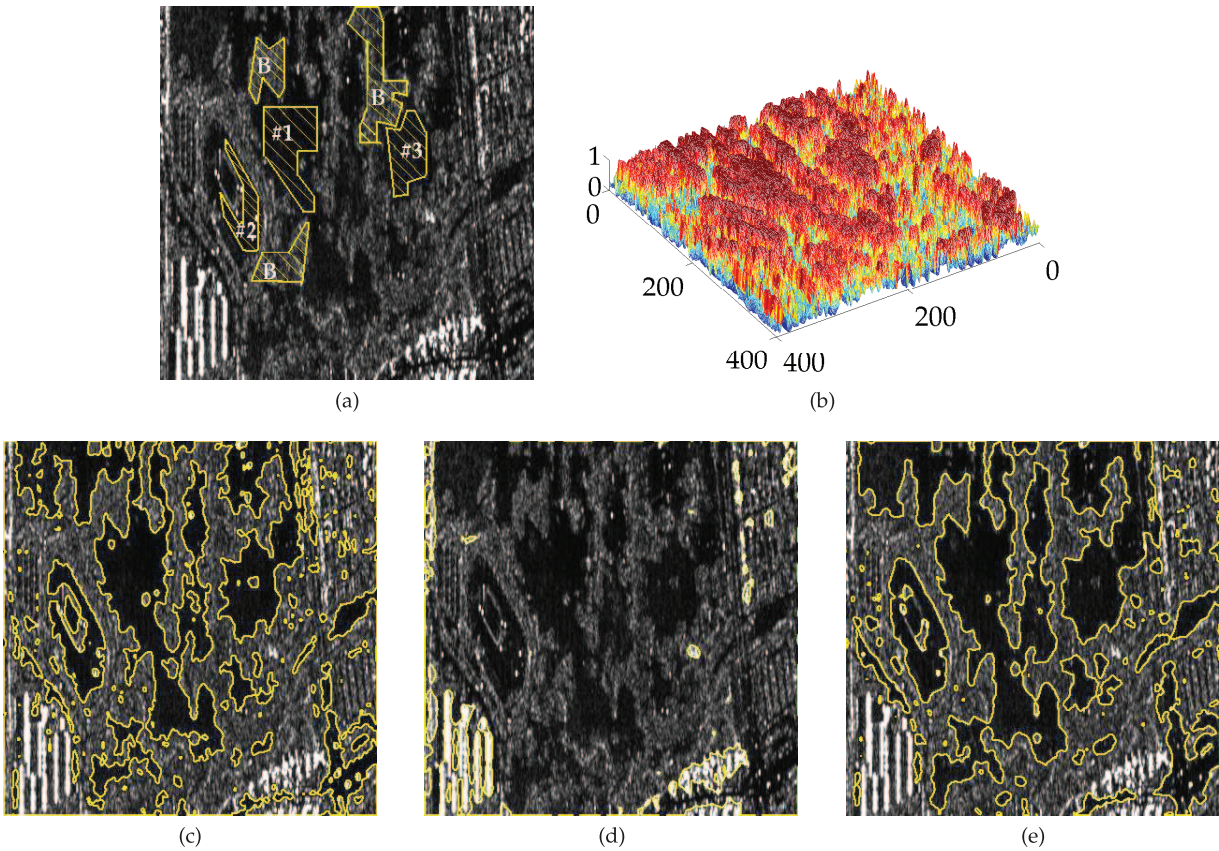


Fig. 8. Segmentation results of a 1-look amplitude SAR image: (a) original image with selected samples, (b) energy map, (c) proposed method result, and (d)-(e) results of the methods in [16] and [37], respectively.

TABLE 4
Evaluation of Segmentation Results in Fig. 8

Region	Estimated parameters of samples in Fig. 8a			CRF		
	$\hat{\alpha}$	$\hat{\gamma}$	DoS	[16]	[37]	Proposed Method
#1	-1.7149	8530.774	10.8264	-	0.5414	0.6223
#2	-1.7563	3339.237	24.8170	-	0.6019	0.6557
#3	-1.8106	4461.011	9.3149	-	0.5337	0.6197
Background	-2.1891	3019.605				

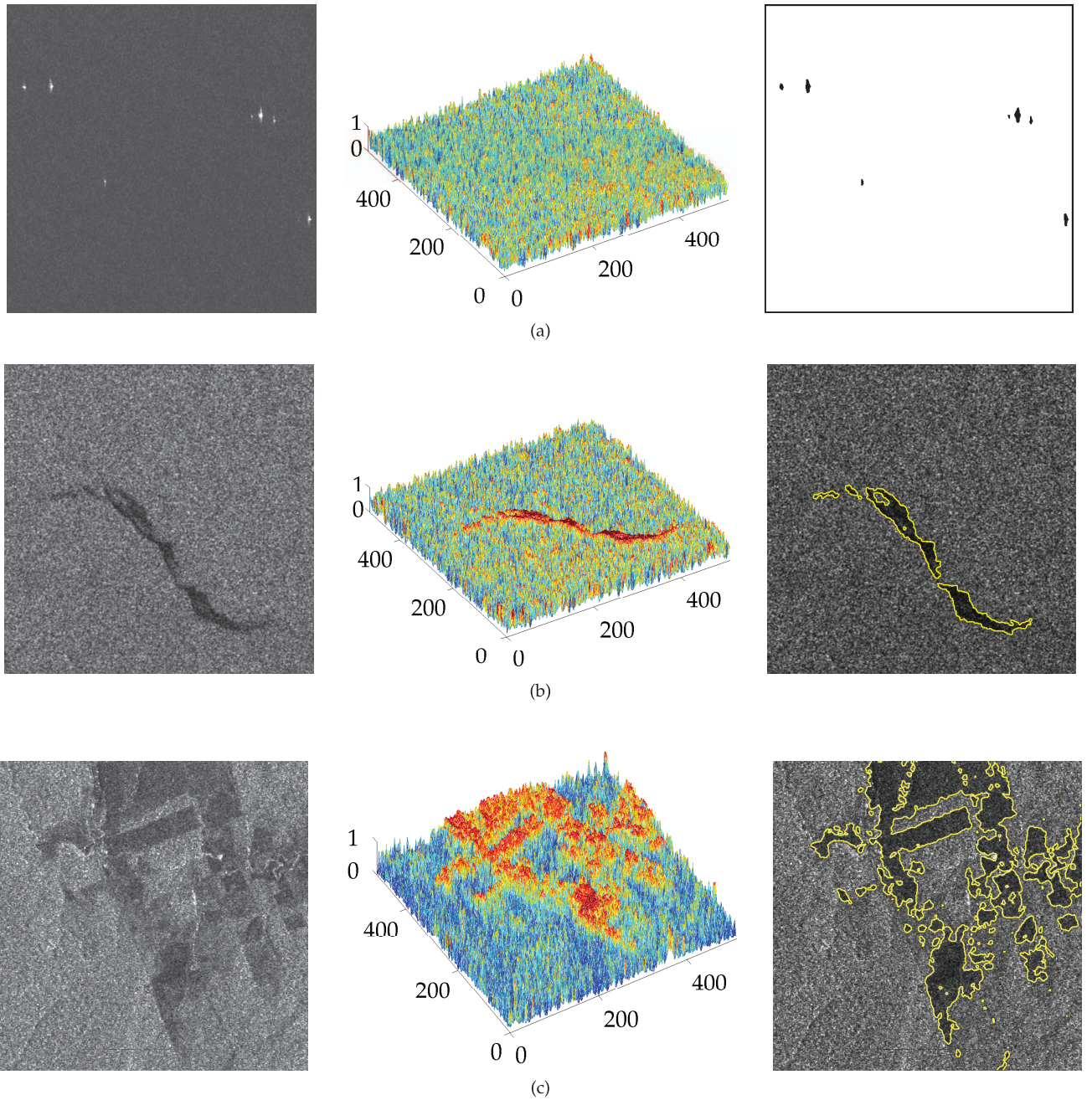


Fig. 9. Real SAR data results of the proposed method. From left to right: SAR image, energy map, and proposed method result of (a)-(b) 4-look amplitude SAR image and (c) 3-look amplitude SAR image.

convergence criterion has avoided excessive computation cost and consistent results were achieved.

4.2 Real SAR Image Segmentation

The proposed method was applied to real single-look and multilook amplitude SAR images. Fig. 8a shows a real 1-look image obtained by ESAR sensor, and Fig. 8b displays its energy map. We have collected samples of different regions to perform stochastic assessment based on estimated parameters. These results are presented in Table 4, and it is worth emphasizing the selected samples were the same applied to all methods to allow a reliable analysis.

In accordance with the *DoS* measure, we can conclude that region #2 in Fig. 8a configured a challenge for the

segmentation algorithm due to the minimal contrast variation when compared to the background. In general, our method presented the best results for the background-foreground separability, according to *CRF* values.

Figs. 9a and 9b display images that were acquired with 4-look and 2 bytes per pixel resolution by the RADARSAT satellite and both subscenes are of 512×512 pixels. Fig. 9a presents bright targets that are identified as offshore oil platforms, and Fig. 9b shows an oil slick in the Brazilian northeast coast. Fig. 9c displays a 3-look SAR image that was obtained by JERS sensor over the Brazilian Amazon. The dark areas in this image are classified as secondary and clear-cut forest. The results displayed in Fig. 9 suggest the proposed approach produced satisfactory results when

TABLE 5
Evaluation of Segmentation Results in Fig. 9

Region	DoS	CRF Method	
		introduced in [37]	proposed
Targets	9.769e14	-	0.697
Oil slick	2.104e18	0.549	0.557
Clear-cut forest	0.751e03	0.753	0.791

segmenting bright points, small regions, and low contrast scenes. Table 5 summarizes comparative results of images displayed in Fig. 9. The oil slick image in Fig. 9b presented $DoS = 2.1e18$, which configures the more hard test. According to CRF index, the proposed method presented the most inferior segmentation error. Furthermore, these results show our technique succeeded in segmenting different targets.

In fact, the proposed approach has presented interesting results for target detection tests. Accordingly, target energy maps demonstrated the discrimination capability of the proposed functional to achieve SAR region characterization. Thus, the segmentation process can be interpreted as an energy band partition, especially for high and low-energy values.

5 CONCLUDING REMARKS AND FURTHER WORKS

In this paper, we have introduced a level set segmentation method with a propagation model that incorporates speckle statistics of amplitude SAR data. Furthermore, we derived an energy functional that arises from a statistical model for SAR data that encompasses the \mathcal{G}_A^0 law and its parameters. This functional is used to drive the level sets to segment homogeneous and heterogeneous regions. These different SAR regions are discriminated according to low and high-energy values of this functional.

The experimental results included tests with synthetic and real SAR images and showed the accuracy of the proposed method. From the Monte Carlo experiments, we observed that the algorithm performed satisfactorily for 93 percent of experiments, using the same set of level set parameters. In addition, the proposed evaluation methodology results were consistent with the RFE index, which demonstrates that stochastic measures based on noise statistics are promising assessment tools.

Further work will investigate the applicability of the proposed energy functional in SAR image filtering and classification tasks. In addition, different energy functionals can be derived from other statistical models, as the ones assigned to polarimetric SAR images.

ACKNOWLEDGMENTS

The authors gratefully acknowledge Daniela M. Ushizima from Lawrence Berkeley National Laboratory for the enlightening suggestions. They are also grateful to the reviewers for their valuable comments, which greatly improved the quality of this paper.

REFERENCES

[1] J.C. Culander and R.N. McDounough, *Synthetic Aperture Radar: Systems and Signal Processing*. John Wiley & Sons, 1991.

[2] J.S. Lee, "Speckle Analysis and Smoothing of Synthetic Aperture Radar Images," *Computer Graphics and Image Processing*, vol. 17, pp. 24-32, 1981.

[3] V.S. Frost, J.A. Stiles, K.S. Shanmugan, and J.C. Holstzman, "A Model for Radar Image and Its Application to Adaptive Digital Filtering of Multiplicative Noise," *IEEE Trans. Pattern Analysis and Machine Intelligence*, vol. 4, no. 2, pp. 157-166, Mar. 1982.

[4] D.T. Kuan, A.A. Sawchuk, T.C. Strand, and P. Chavel, "Adaptive Noise Smoothing Filter for Images with Signal Dependent Noise," *IEEE Trans. Pattern Analysis and Machine Intelligence*, vol. 7, no. 2, pp. 165-177, Mar. 1985.

[5] C. Li, "Two Adaptive Filters for Speckle Reduction in SAR Images by Using the Variance Ratio," *Int'l J. Remote Sensing*, vol. 9, no. 4, pp. 641-653, 1988.

[6] A. Lopes, E. Nezry, R. Touzi, and H. Laur, "Structure Detection and Statistical Adaptive Speckle in SAR Images," *Int'l J. Remote Sensing*, vol. 14, no. 9, pp. 1735-1758, June 1993.

[7] J.M. Park, W.J. Song, and W.A. Pearlman, "Speckle Filtering of SAR Images Based on Adaptive Windowing," *IEE Proc. Vision, Image and Signal Processing*, vol. 146, no. 33, pp. 191-197, Aug. 1999.

[8] J.S. Lee, J.-H. Wen, T.L. Ainsworth, K.-S. Chen, and A.J. Chen, "Improved Sigma Filter for Speckle Filtering of SAR Imagery," *IEEE Trans. Geoscience Remote Sensing*, vol. 47, no. 1, pp. 202-213, Jan. 2009.

[9] S. Huang, D.Z. Liu, G.Q. Gao, and X.J. Guo, "A Novel Method for Speckle Noise Reduction and Ship Target Detection in SAR Images," *Pattern Recognition*, vol. 42, pp. 1533-1542, 2009.

[10] L. Denis, F. Tupin, J. Darbon, and M. Sigelle, "SAR Image Regularization with Fast Approximate Discrete Minimization," *IEEE Trans. Image Processing*, vol. 18, no. 7, pp. 1588-1600, July 2009.

[11] J.A. Sethian, *Level Set Methods and Fast Marching Methods: Evolving Interfaces in Computational Geometry, Fluid Mechanics, Computer Vision and Materials Science*. Cambridge Univ. Press, 1998.

[12] T. Riklin-Raviv, N. Sochen, and N. Kiryati, "On Symmetry, Perspectivity and Level-Set-Based Segmentation," *IEEE Trans. Pattern Analysis and Machine Intelligence*, vol. 31, no. 8, pp. 1458-1471, Aug. 2009.

[13] C.M. Li, C.Y. Xu, C.F. Gui, and M.D. Fox, "Level Set Evolution without Re-Initialization: A New Variational Formulation," *Proc. IEEE Conf. Computer Vision and Pattern Recognition*, pp. 430-436, June 2005.

[14] Y. Shi and W.C. Karl, "Real-Time Tracking Using Level Sets," *Proc. IEEE Conf. Computer Vision and Pattern Recognition*, pp. 34-41, June 2005.

[15] S. Chitroub, A. Houacine, and B. Sansal, "Statistical Characterisation and Modelling of SAR Images," *Signal Processing*, vol. 82, pp. 69-92, 2002.

[16] I.B. Ayed, A. Mitiche, and Z. Belhadj, "Multiregion Level-Set Partitioning of Synthetic Aperture Radar Images," *IEEE Trans. Pattern Analysis and Machine Intelligence*, vol. 27, no. 5, pp. 793-800, May 2005.

[17] Y. Shuai and H. Sun, "SAR Image Segmentation Based on Level Set with Stationary Global Minimum," *IEEE Geoscience and Remote Sensing Letters*, vol. 5, no. 4, pp. 644-648, Oct. 2008.

[18] R.C.P. Marques, F.N.S. Medeiros, and D.M. Ushizima, "Target Detection in SAR Images Based on a Level Set Approach," *IEEE Trans. Systems, Man, and Cybernetics C: Applications and Rev.*, vol. 39, no. 2, pp. 214-222, Mar. 2009.

[19] A.C. Frery, H.-J. Müller, C.C. Freitas, and S.J.S. Sant'Anna, "A Model for Extremely Heterogeneous Clutter," *IEEE Trans. Geoscience and Remote Sensing*, vol. 35, no. 3, pp. 648-659, May 1997.

[20] G. Gao, "Statistical Modeling of SAR Images: A Survey," *Sensors*, vol. 10, pp. 775-795, 2010.

[21] M.E. Mejail, J. Jacobo, A.C. Frery, and O.H. Bustos, "Classification of SAR Images Using a General and Tractable Multiplicative Model," *Int'l J. Remote Sensing*, vol. 24, no. 18, pp. 3565-3582, 2003.

[22] J. Gambini, J. Jacobo, and A.C. Frery, "Feature Extraction in Speckled Imagery Using Dynamic B-Spline Deformable Contours under the \mathcal{G}_A^0 Models," *Int'l J. Remote Sensing*, vol. 27, no. 22, pp. 5037-5059, 2006.

[23] J. Gambini, M.E. Mejail, J. Jacobo, and A.C. Frery, "Accuracy of Edge Detection Methods with Local Information in Speckled Imagery," *Statistics and Computing*, vol. 18, no. 1, pp. 15-26, 2008.

[24] O.H. Bustos, M.M. Lucini, and A.C. Frery, "M-Estimators of Roughness and Scale for \mathcal{G}_A^0 -Modelled SAR Imagery," *J. Applied Signal Processing*, vol. 1, pp. 105-114, 2002.

- [25] A.C. Frery, A.H. Correia, and C.C. Freitas, "Classifying Multi-frequency Fully Polarimetric Imagery with Multiple Sources of Statistical Evidence and Contextual Information," *IEEE Trans. Geoscience and Remote Sensing*, vol. 45, no. 10, pp. 3098-3109, Oct. 2007.
- [26] C.C.F. Yanasse, A.C. Frery, and S.S. Sant'Anna, "Stochastic Distributions and the Multiplicative Model: Relations, Properties, Estimators and Applications to SAR Image Analysis," Technical Report 5630-NTC/318, INPE, ed. São José dos Campos, São Paulo, Brazil, 1995.
- [27] H. Allende, A.C. Frery, J. Galbiati, and L. Pizarro, "M-Estimators with Asymmetric Influence Functions: The \mathcal{G}_A^0 Distribution Case," *J. Statistical Computation and Simulation*, vol. 76, no. 11, pp. 941-956, 2006.
- [28] A.C. Frery, F. Cribari-Neto, and M.O. de Souza, "Analysis of Minute Features in Speckled Imagery with Maximum Likelihood Estimation," *EURASIP J. Applied Signal Processing*, vol. 2004, pp. 2476-2491, 2004.
- [29] P.K. Sen, J.M. Singer, and A.C.P. Lima, *From Finite Sample to Asymptotic Methods in Statistics*, first ed. Cambridge Univ. Press, 2010.
- [30] A.C. Davison and D.V. Hinkley, *Bootstrap Methods and Their Application*, first ed. Cambridge Univ. Press, 1997.
- [31] A.C. Frery, A.D.C. Nascimento, and R.J. Cintra, "Contrast in Speckled Imagery with Stochastic Distances," *Proc. IEEE 17th Int'l Conf. Image Processing*, pp. 69-72, Sept. 2010.
- [32] D. Mumford and J. Shah, "Optimal Approximations by Piecewise Smooth Functions and Associated Variational Problems," *Comm. Pure and Applied Math.*, vol. 42, pp. 577-685, 1989.
- [33] G. Zhu, S. Zhang, Q. Zeng, and C. Wang, "Boundary-Based Image Segmentation Using Binary Level Set Method," *SPIE OE Letters*, vol. 46, 2007.
- [34] K. Zhang, H. Song, and L. Zhang, "Active Contours Driven by Local Image Fitting Energy," *Pattern Recognition*, vol. 43, pp. 1199-1206, 2010.
- [35] A.D.C. Nascimento, R.J. Cintra, and A.C. Frery, "Hypothesis Testing in Speckle Data with Stochastic Distances," *IEEE Trans. Geoscience Remote Sensing*, vol. 48, no. 1, pp. 373-385, Jan. 2010.
- [36] E.V.D. Lucca, C.C. Freitas, A.C. Frery, and S.J.S. Sant'Anna, "Comparison of SAR Segmentation Algorithms," *Proc. IX Brazilian Symp. Remote Sensing*, pp. 1097-1108, 1998.
- [37] X. Huang, B. Huang, and H. Li, "A Fast Level Set Method for Synthetic Aperture Radar Ocean Image Segmentation," *Sensors*, vol. 9, pp. 814-829, 2009.



Regis C. Pinheiro Marques received the BSc and the MSc degrees in electrical engineering from Federal University of Ceara (UFC), Fortaleza, Brazil, in 2003 and 2004, respectively. He is currently working toward the PhD degree in teleinformatics engineering at UFC. Since 2000, he has been working in the Vision, Images and Signal Laboratory (LABVIS) at UFC. In 2005, he joined the Telematics Department of the Federal Institute of Education, Science and

Technology (IFCE) as a professor. His main research interests are SAR data modeling, level set methods, image filtering, and segmentation.



Fátima N. Sombra de Medeiros received the BSc degree in electrical engineering from the Federal University of Ceara (UFC), the MSc degree in electrical engineering from the Pontifical Catholic University of Rio de Janeiro (PUC-RJ) in 1988, and the PhD degree in computational physics from the Physics Institute, University of São Paulo (USP) in 1999. She is currently a full professor in the Teleinformatics Engineering Department, Federal University of Ceara, Brazil, and head of the Image Processing Research Group. Her main interests include SAR image processing and analysis for remote sensing of environment, shape analysis, and computer vision. She has published journal papers in the *International Journal of Remote Sensing*, *IEEE Transactions on Systems, Man, and Cybernetics*, *EURASIP Journal on Applied Signal Processing*, *Sensors*, *Digital Signal Processing*, among others in international events. She has acted as a reviewer for the *IEEE Signal Processing Letters*, *International Journal of Remote Sensing*, *IEEE Geoscience and Remote Sensing Letters*, *Journal of Mathematical Imaging and Vision*, and *EURASIP Journal on Applied Signal Processing*, among other international events.



Juvencio Santos Nobre received the BSc degree in statistics (magna cum laude) from the Federal University Ceara (UFC) in 2002, the MSc degree in 2004, and the PhD degree in 2007, both in statistics, from the Mathematics and Statistics Institute, University of São Paulo (USP). Since 2006, he has been a full professor in the Statistics and Applied Mathematics Department, Federal University of Ceara. His main research interests are analysis of repeated

measures, large sample theory, constrained inference, semiparametric and nonparametric methods, bootstrap methods, diagnostics methods for regression models, and statistics analysis of images.

► For more information on this or any other computing topic, please visit our Digital Library at www.computer.org/publications/dlib.